Available online at www.sciencedirect.com
ScienceDirect
International Journal of Heat and Mass Transfer 51 (2008) 4315–4326
International Journal of HEAT and MASS TRANSFER
www.elsevier.com/locate/ijhmt

Fluid flow and heat transfer characteristics of low temperature two-phase micro-channel heat sinks – Part 1: Experimental methods and flow visualization results

Jaeseon Lee, Issam Mudawar *

Boiling and Two-Phase Flow Laboratory (BTPFL), Purdue University International Electronic Cooling Alliance (PUIECA), Mechanical Engineering Building, 585 Purdue Mall, West Lafayette, IN 47907-2088, USA

Received 13 June 2007; received in revised form 16 February 2008
Available online 9 May 2008

Abstract

A new cooling scheme is proposed where the primary working fluid flowing through a micro-channel heat sink is pre-cooled to low temperature using an indirect refrigeration cooling system. Cooling performance was explored using HFE 7100 as working fluid and four different micro-channel sizes. High-speed video imaging was employed to help explain the complex interrelated influences of hydraulic diameter, micro-channel width, mass velocity and subcooling on cooling performance. Unlike most prior two-phase micro-channel heat sink studies, which involved annular film evaporation due high void fraction, the low coolant temperatures used in this study produced subcooled flow boiling conditions. Decreasing coolant temperature delayed the onset of boiling, reduced bubble size and coalescence effects, and enhanced CHF. Heat fluxes in excess of 700 W/cm^2 could be managed without burnout. Premature CHF occurred at low mass velocities and was caused by vapor flow reversal toward the inlet plenum. This form of CHF was eliminated by decreasing coolant temperature and/or increasing flow rate.

1. Introduction

Aggressive pursuit of faster signal speed and superior performance of electronic devices has precipitated unprecedented increases in heat dissipation at all levels of electronics packaging, device, module and system. New innovative cooling methods are therefore required to remove the dissipated heat. Today, localized heat dissipation from advanced microprocessors has already exceeded 100 W/cm^2, while high-end defense applications such as lasers, microwave devices, and radars are beginning to exceed 1000 W/cm^2 [1]. Another primary function of an electronics cooling system is to maintain device temperature below a limit that is set by both material and reliability concerns. This limit varies with application, from 85 °C for commercial microprocessors to about 125 °C for defense electronics [1].

A high-flux liquid-cooled electronic module can be characterized by an overall thermal resistance between device and ambient (typically room air). This resistance is the sum of all conductive resistances of materials comprising the electronic package as well as the convective resistances of coolant internal to the package as well as the ultimate ambient cooling fluid. Advances in both material and packaging have greatly reduced the overall thermal resistance of the package. Similar aggressive efforts are underway to reduce the internal convective resistance using such powerful cooling schemes as micro-channel flow and jet impingement, especially where the coolant undergoes phase change.

The difficulty implementing even the most aggressive and powerful cooling schemes is that, for fixed overall resistance and ambient temperature, device temperature increases fairly linearly with increasing heat dissipation

* Corresponding author. Tel.: +1 765 494 5705; fax: +1 765 494 0539.
E-mail address: mudawar@ecn.purdue.edu (I. Mudawar).

0017-9310/$ - see front matter © 2008 Elsevier Ltd. All rights reserved.
doi:10.1016/j.ijheatmasstransfer.2008.02.012

Nomenclature

AR	aspect ratio of micro-channel
CHF	critical heat flux
c_p	specific heat
D_h	hydraulic diameter of micro-channel
G	mass velocity
h	enthalpy
H_{ch}	micro-channel height
h_{fg}	latent heat of vaporization
H_{tc}	distance between thermocouple and bottom wall of micro-channel
k	thermal conductivity
L	length of micro-channel
L_{tc}	axial location of copper block thermocouple
$\dot{m}$	total coolant mass flow rate of micro-channel heat sink
N	number of micro-channels in test section
P	pressure
q''	heat flux based on total base area of micro-channel heat sink
Re_{Dh}	Reynolds number based on hydraulic diameter
T	temperature
T_{tc}	measured copper block temperature
T_w	bottom wall temperature of micro-channel
$\overline{T}_w$	mean bottom wall temperature of micro-channel
TS	test section
W_{ch}	micro-channel width
W_w	half-width of copper wall separating micro-channels
x	coordinate defined in Fig. 4
y	coordinate defined in Fig. 4
z	stream-wise coordinate

Greek symbols

μ	viscosity
ρ	density
σ	surface tension
ϕ	fluid phase indicator

Subscripts

1, 2, 3	measurement location
ch	micro-channel
f	liquid
g	saturated vapor
in	test section inlet
out	test section outlet
sat	saturated
tc	thermocouple
w	bottom wall of micro-channel.

rate. This relationship is especially problematic for defense electronics, where dissipating say 1000 W/cm^2 would bring the device well above its maximum temperature limit. To circumvent this problem, direct or indirect low temperature cooling systems could facilitate appreciable reduction in the temperature of coolant inside the electronic package, and, hence, in the temperature of the device itself.

During the past few years, there has been a noticeable increase in the number of commercial systems that capitalize on low temperature cooling [2,3]. The most popular of those is the vapor compression refrigeration system, which features high mechanical reliability and good ratio of temperature drop to thermal capacity. Even lower temperatures are possible with cryogenic cooling systems such as Joule–Thomson, Stirling cycle, pulse tube, thermo-acoustic, Gifford McMahon and submerged liquid cryogen. Aside from their cooling merits, cryogenic temperatures provide the benefits of better reliability and enhanced performance [4]. In fact, much faster switching time has been clocked with devices at 100 K compared to those at above ambient temperature. However, a key drawback to cryogenic cooling systems is very low thermal capacity, let alone high cost. These drawbacks render vapor compression systems the most feasible choice for applications demanding low temperature cooling. These systems possess good thermal capacity and can yield cooling temperatures down to −100 °C.

Two types of refrigeration cooling systems are possible. The first involves incorporating the cooling module as an evaporator in the vapor compression cycle. In other words, the refrigerant serves as primary coolant for the electronic device. This configuration can be classified as *direct refrigeration cooling*. The second involves rejecting the heat from the primary coolant via a heat exchanger to refrigerant flowing in a separate vapor compression cycle. This configuration can be classified as *indirect refrigeration cooling*, and is the focus of the present study.

Recently, the authors of the present study proposed a new direct refrigeration cooling system incorporating a micro-channel evaporator inside which the electronic device is cooled by the refrigerant [5–7]. Using R-134a as working fluid, their study yielded convective heat transfer coefficients comparable to those for water, which has far better thermal transport properties than R-134a [6]. However, compromises had to be made between enhancing the evaporator's cooling performance and the performance of the system as a whole. On one hand, enhancing the evaporator's thermal performance while avoiding dryout favors reducing the evaporator's exit quality. However, this may compromise the performance of the compressor, which favors dry superheated evaporator exit conditions [6]. A practical solution was recommended that involved the use of a thermal load control device (*e.g.*, thermostatic expansion valve) to ensure only slightly superheated vapor conditions at the compressor inlet.

The present two-part study concerns the second, indirect refrigeration cooling configuration. A key advantage of

this configuration over the direct refrigeration configuration is that it decouples the quality requirements of the micro-channel heat sink from those of the compressor in the vapor compression cycle. Three advantages are readily realized with this decoupling. First, the aforementioned compressor problems are completely eliminated. Second, by sizing the vapor compression cycle separately, the cooling system can be designed to simultaneously handle both the required heat rejection capacity and heat rejection temperature. Thirdly, coolant in the electronic module does not need to be highly pressurized; this greatly simplifies the structural design of the module as well as reduces cost. The present study centers on the performance of the micro-channel heat sink using a properly sized indirect refrigeration cooling system.

Using indirect refrigeration cooling, there is greater control over two-phase behavior inside the micro-channel. While two-phase flow inside a direct-refrigeration-cooled micro-channel evaporator is predominantly annular, indirect cooling can maintain even highly subcooled flow boiling conditions, which can enhance convective heat transfer coefficient and delay critical heat flux (CHF).

The first part of this study describes the indirect refrigeration cooling system and experimental methods used. Also discussed in this part is flow boiling behavior that is captured with the aid of high-speed video imaging and photomicrography. Using four differently sized micro-channel heat sinks and broad ranges of operating conditions, the captured two-phase behavior is used to identify dominant mechanisms at heat fluxes up to and including CHF. This behavior is also used in the second part of the study for assessment of existing pressure drop and heat transfer coefficient correlations and models and development of new correlations.

2. Experimental methods

2.1. Indirect refrigeration cooling system

Fig. 1 shows a flow diagram for this newly proposed indirect refrigeration cooling scheme. As indicated earlier, the vapor compression system is completely isolated from the primary cooling loop containing the micro-channel module.

The working fluid in the primary cooling loop is HFE 7100. This 3 M Novec fluid has very low freezing point below −100 °C and a relatively moderate boiling point of 60 °C at atmospheric pressure. Like other phase change electronic cooling fluids (*e.g.*, FC-72 and FC-87), HFE 7100 has excellent dielectric properties, is very inert, and its surface tension is much smaller than that of water. But while its shares the zero ozone depletion potential of

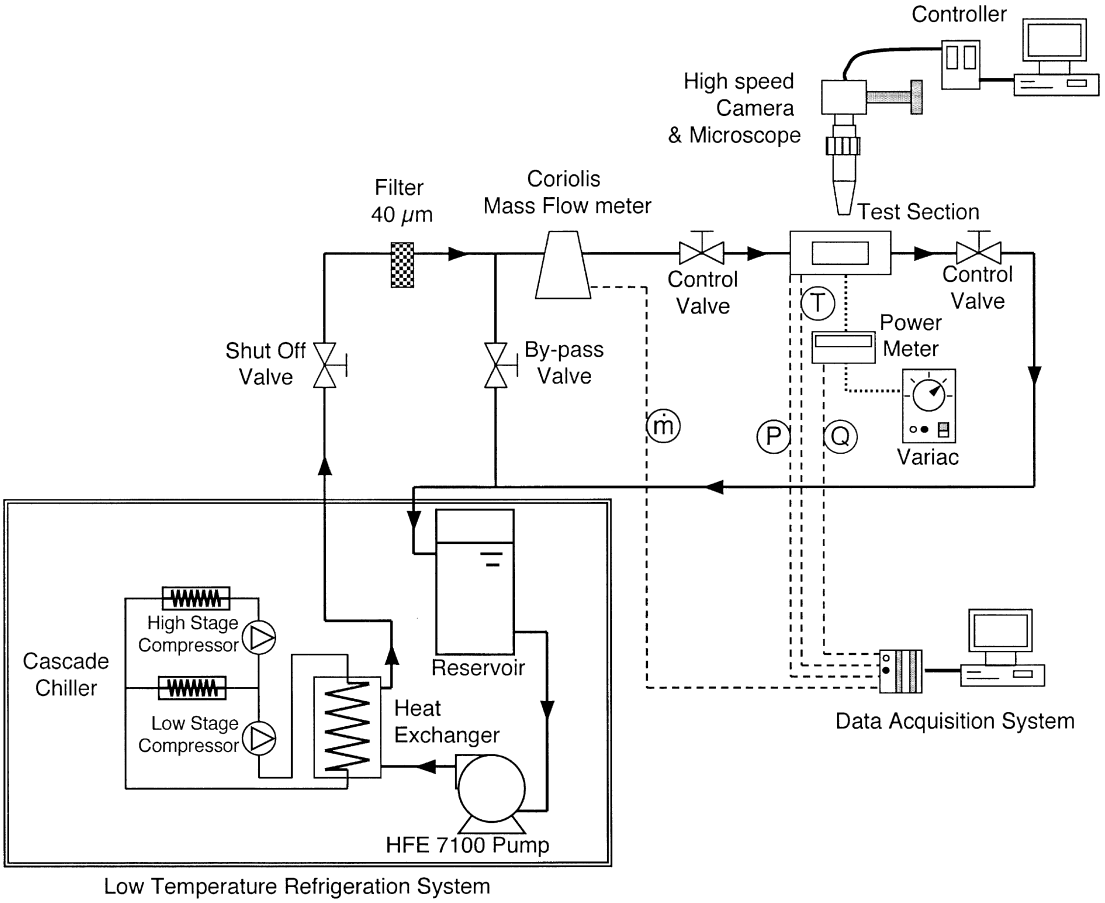

Fig. 1. Flow diagram for indirect refrigeration cooling system.

recent dielectric coolants, HFE 7100 as well as the entire Novec family of coolants also have unusually low global warming potential. Table 1 provides representative values for thermophysical properties of HFE 7100.

As shown in Fig. 1, HFE 7100 is circulated from a reservoir through the primary loop with the aid of a centrifugal pump. This primary fluid passes through a heat exchanger where its temperature is greatly reduced by rejecting heat to the secondary refrigeration loop. Exiting the heat exchanger, the primary fluid passes through a filter followed by a Coriolis mass flow meter before entering the micro-channel test section. Throttling valves situated both upstream and downstream of the test section are used to control both flow rate and exit pressure. Exiting the downstream valve, the primary coolant is returned to reservoir. Fig. 1 highlights the aforementioned practical advantage of an indirect refrigeration cooling system. Because the primary and refrigeration loops are completely isolated, the micro-channel test section maintains only a mild operating pressure, which is advantageous for electronics cooling applications.

Table 1
Summary of thermophysical properties of HFE 7100

	k_f (W/m K)	μ_f (kg/m s)	$c_{p,f}$ (kJ/kg K)	σ (mN/m)
$T = -30$ °C	0.0796	14.74×10^{-4}	1073.0	18.2
$T = 0$ °C	0.0737	8.26×10^{-4}	1133.0	15.7

	T_{sat} (°C)	h_f (kJ/kg)	h_{fg} (kJ/kg)	ρ_f (kg/m^3)	ρ_g (kg/m^3)
$P = 1.0$ bar	59.63	92.76	111.7	1372.7	9.58
$P = 3.5$ bar	104.41	145.5	97.61	1238.9	32.14

To achieve high cooling capacity at low temperatures, a cascade cycle is used in the refrigeration system. This two-stage compression system employs two different refrigerants, R507 for the high compression stage and R508b for the lower stage. With this cascade feature, the system is capable of rejecting 550 W at −80 °C and its capacity increases with increasing temperature. Another feature of this system is its ability to maintain the temperature of HFE 7100 in the primary loop at the heat exchanger outlet to within ±0.5 °C using automatic feedback control.

2.2. Micro-channel test section

Fig. 2 illustrates the construction of the micro-channel test section. Micro-channels with rectangular cross-section are formed by micro-slotting the top surface of an oxygen-free copper block with the aid of a series of thin carbide blades. The enlarged underside of the copper block has four bores to accommodate high-power-density cartridge heaters. The top portion of the copper block is inserted into a rectangular housing made from G-11 fiberglass plastic which is suitable for both low and high temperature operation. This housing features coolant inlet and outlet ports, micro-channel inlet and outlet plenums, and both pressure and temperature instrumentation ports. The micro-channels are formed by clamping a polycarbonate plastic cover

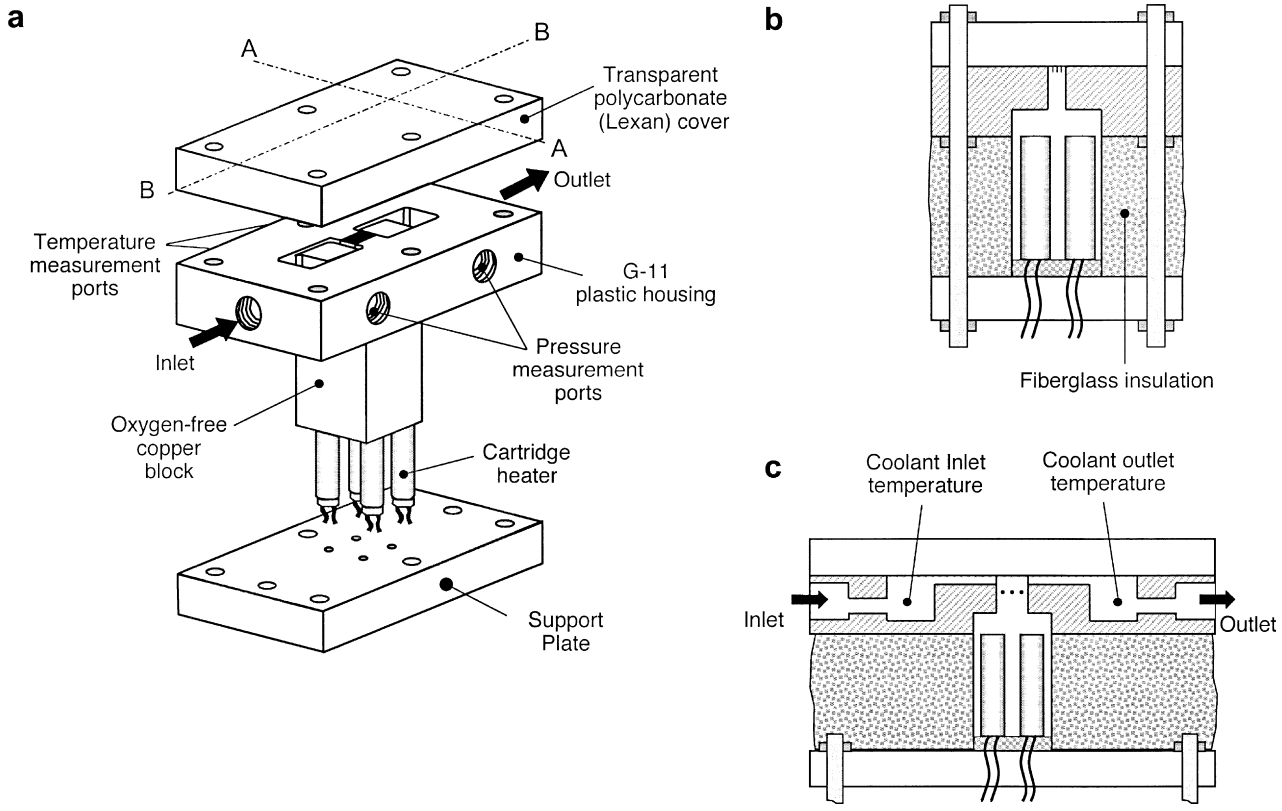

Fig. 2. (a) Isometric view of micro-channel test section. (b) Cross-sectional view (A–A). (c) Side sectional view (B–B).

plate atop the housing and the copper block. The transparent cover plate provides top viewing access to the flow inside the micro-channels. All other surfaces of the copper block are carefully insulated to minimize heat loss to the ambient.

To examine the effects of micro-channel hydraulic diameter and aspect ratio, four different copper blocks were machined, each containing different micro-channel features. All four copper blocks have the same top 0.5 cm wide by 1.0 cm long heat transfer area. Dimensions of the four test sections are given in Table 2. Fig. 3 shows microscope images of the micro-channels in each test section.

2.3. Operating conditions and measurements

As indicated earlier, the indirect refrigeration cooling system ensured the delivery of primary coolant (HFE 7100) to the micro-channel test section at precise temperature using automated feedback control. Tests were performed at two test module inlet temperatures, −30 and 0 °C. Lower temperatures were possible but avoided because frost on the test section's transparent cover plate disrupted optical access below −30 °C.

Table 2
Test section dimensions

	W_{ch} (μm)	W_w (μm)	H_{ch} (μm)	AR	D_h (μm)	L (cm)	N
TS #1	123.4	84.2	304.9	2.47	175.7	1.0	24
TS #2	123.4	84.6	526.9	4.27	200.0	1.0	24
TS #3	235.2	230.3	576.8	2.45	334.1	1.0	11
TS #4	259.9	205.0	1041.3	4.01	415.9	1.0	11

Aside from inlet temperature, the test matrix for the present study included variations of flow rate of the primary coolant and heat flux; a constant test section's outlet pressure of 1.138 bar was maintained throughout the study. Table 3 provides ranges of key parameters of the study for each of the four test sections.

The test section's instrumentation included pressure transducers and thermocouples for both the inlet and outlet plenums. Three type-T thermocouples were inserted in the copper block beneath the micro-channels as illustrated in Fig. 4. The thermocouple measurements ($T_{tc,1}$, $T_{tc,2}$, $T_{tc,3}$) enabled the calculation of heat transfer coefficients and wall temperatures at the base of the micro-channel ($T_{w,1}$, $T_{w,2}$, $T_{w,3}$) immediately above using a fin analysis method and the assumption of 1-D vertical conduction as discussed in Refs. [6–9]. Other measurements included electrical power input to the test section's four cartridge heaters using a Wattmeter, and mass flow rate using the Coriolis flow meter. All measurements were made simultaneously and processed by an HP3852 data acquisition system.

2.4. Measurement uncertainty

A primary concern in the present study was to accurately determine the heat flux supplied to the primary coolant. Despite the large convective heat transfer coefficient inside the micro-channels, relatively small wetted area compared to overall surface area of the copper block was a reason for concern over potentially large heat loss. For single-phase flows, this heat loss can be easily determined by comparing the fluid's sensible heat rise to the electrical power input.

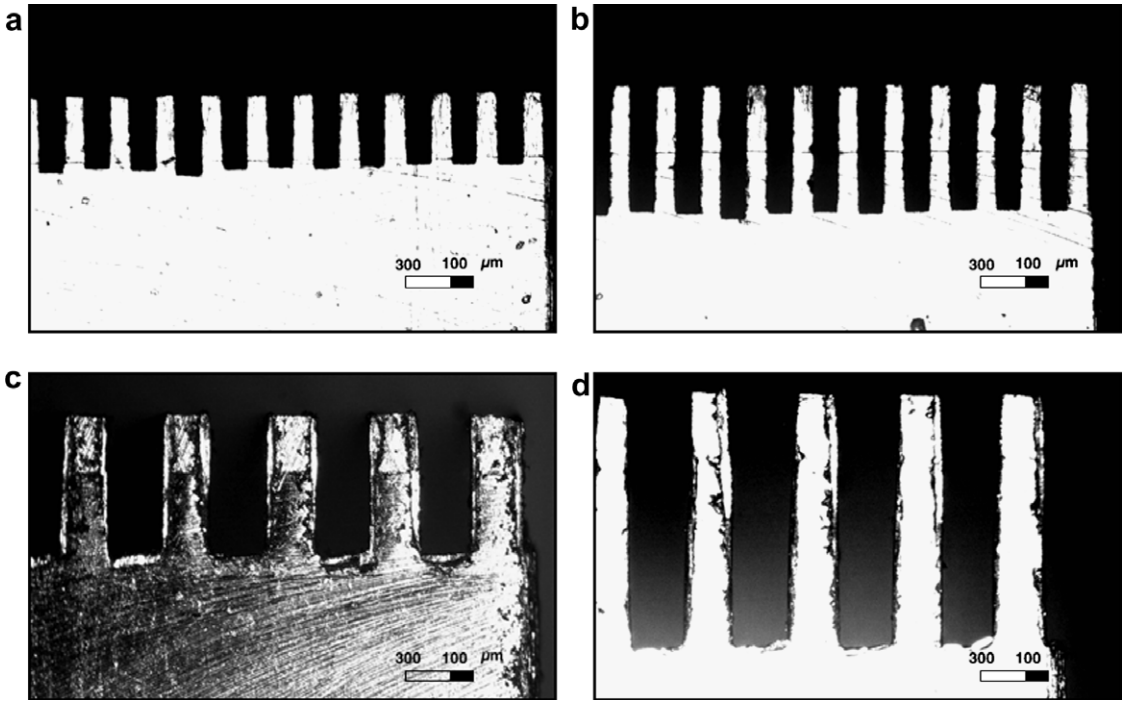

Fig. 3. Microscope images of micro-channels: (a) TS #1 ($D_h = 175.7$ μm), (b) TS #2 ($D_h = 200.0$ μm), (c) TS #3 ($D_h = 334.1$ μm), and (d) TS #4 ($D_h = 415.9$ μm).

Table 3
Experimental operating conditions

	T_{in} (°C)	$\dot{m}$ (g/s)	P_{out} (bar)	G (kg/m^2 s)	Re_{Dh}	q'' (W/cm^2)
TS #1	−30, 0	2.0–5.0	1.138	2200–5550	265–1170	0–560
TS #2	−30, 0	2.0–5.0	1.138	1280–3210	175–780	0–580
TS #3	−30, 0	2.0–5.0	1.138	1330–3350	304–1360	0–640
TS #4	−30, 0	2.0–20.0	1.138	670–6730	189–3370	0–750

Unfortunately, this method cannot be applied in two-phase situations. Therefore a new method had to be devised to determine the heat loss.

This method involved an iterative calculation scheme. In the first iteration, zero heat loss was assumed and both the convective heat transfer coefficients and wall temperatures inside the micro-channel were calculated at the axial locations of the thermocouples using the aforementioned fin analysis method and the assumption of 1-D vertical conduction. A finite element model was constructed for the entire test section, including housing, cover plate and insulation, which accounted for external natural convection. Boundary conditions for the micro-channel in the finite element model were determined by averaging the three heat transfer coefficient values from the first iteration and using a fluid temperature equal to the average of the measured inlet and outlet temperatures. Heat loss was then estimated using the finite element model. In the second iteration, a new heat flux value was used after deducting heat loss from the total electrical power input. New values of the convective heat transfer coefficients were determined for the three axial locations of thermocouples using the fin analysis method and assumption of 1-D vertical conduction. Using a new average of the three heat transfer coefficient values, the finite element model was used once again to provide an updated estimate of heat loss. Further iteration was attempted until the three heat transfer coefficient values converged. This required about 7–13 iterations depending on test section and operating conditions. With this approach, heat loss was estimated at 14–20% of electrical power input for single-phase conditions, and 6–14% for two-phase conditions. The experimental data presented in this study have all been corrected for this heat loss.

Uncertainties in the temperature measurements were ±0.5 °C for inlet fluid temperature control and ±0.3 °C for thermocouple readings. Accuracies of other measurement instruments were as follows: ±0.5% for the pressure transducers, ±0.1% for the Coriolis flow meter, and ±0.1% for the Wattmeter.

2.5. Photographic methods

Flow visualization played a major role in capturing two-phase flow behavior in the micro-channels. A high-speed digital video imaging system was used for this purpose. Two key requirements for capturing the complex interfacial features in a micro-channel with high resolution are high shutter speed and high magnification. The Photron FASTCAM-Ultima camera system used in the present study is capable of shutter speeds up to 1/120,000 s. However, practical shutter speeds were dictated by lighting requirements. Lighting was provided by a PerkinElmer Xenon source fitted with an Olympus fiber optic cable that focused the light on the photographed region of the micro-channel. The present study employed a shutter speed of

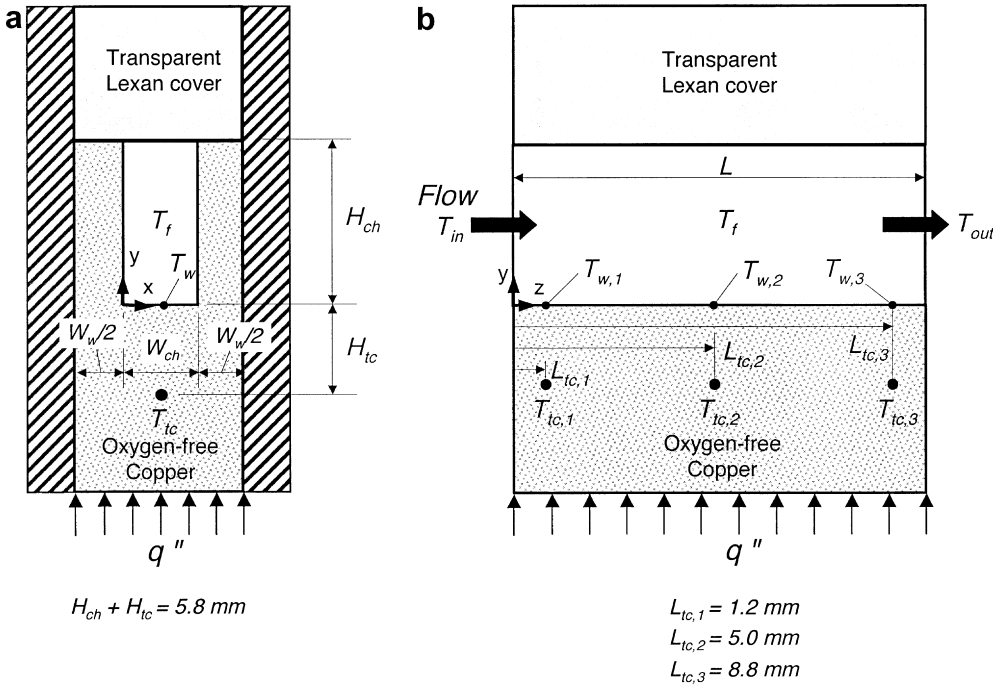

Fig. 4. Micro-channel unit cell and locations of thermocouples in (a) x–y plane and (b) y–z plane.

1/8000 s for relatively slow isolated bubbles and 1/15,000 s for fast and/or coalescing bubbles.

To achieve high magnification, two different Infinity K-2 lenses were used. The first provides 4–5.8 times magnification and a 1.1–1.6 mm field of view. This lens was quite effective for test sections TS #3 and TS #4, capturing 3–4 micro-channels in each test section. The other lens provides 8–10.7 times magnification and a 0.6–0.8 mm field of view. This lens was used with test sections TS #1 and TS #2, which had about half the micro-channel width of TS #3 and TS #4. This second lens captured 7–9 micro-channels in TS #1 and TS #2.

3. Heat transfer results

3.1. Subcooled flow boiling regime

Fig. 5 shows for TS #1 variations of the measured fluid outlet temperature and mean temperature of the micro-channel bottom wall with heat flux for two mass flow rates. Notice how wall temperature is below ambient temperature for fluxes as high as 120 W/cm^2 depending on flow rate; these conditions typically fall into the single-phase region. Fig. 5b shows single-phase cooling sustained well above 200 W/cm^2 for $\dot{m} = 5$ g/s. However, fluid temperature for both flow rates never reached saturation. This is especially the case for the higher flow rate. This indicates subcooled boiling conditions prevail inside the test section for both flow rates. The outlet temperature data suggest highly subcooled boiling conditions for the higher flow rate. This shows that with indirect refrigeration cooling subcooled boiling can be achieved even at very high fluxes.

In fact, subcooled boiling prevailed for almost all operating conditions of the present study, regardless of test section. What was different among the different operating conditions was the degree of subcooling inside the micro-channels. This issue will become more apparent from the video images discussed below.

From a modeling standpoint, subcooled boiling poses major challenges, particularly in terms of the ability to predict void fraction and pressure drop. Interestingly, most of the published literature on two-phase micro-channel heat sinks concerns saturated boiling, where annual flow is dominant. The complexity of the present situation warrants careful assessment of interfacial interactions inside the micro-channel heat sink. In fact, this is the primary goal of this first part of the study.

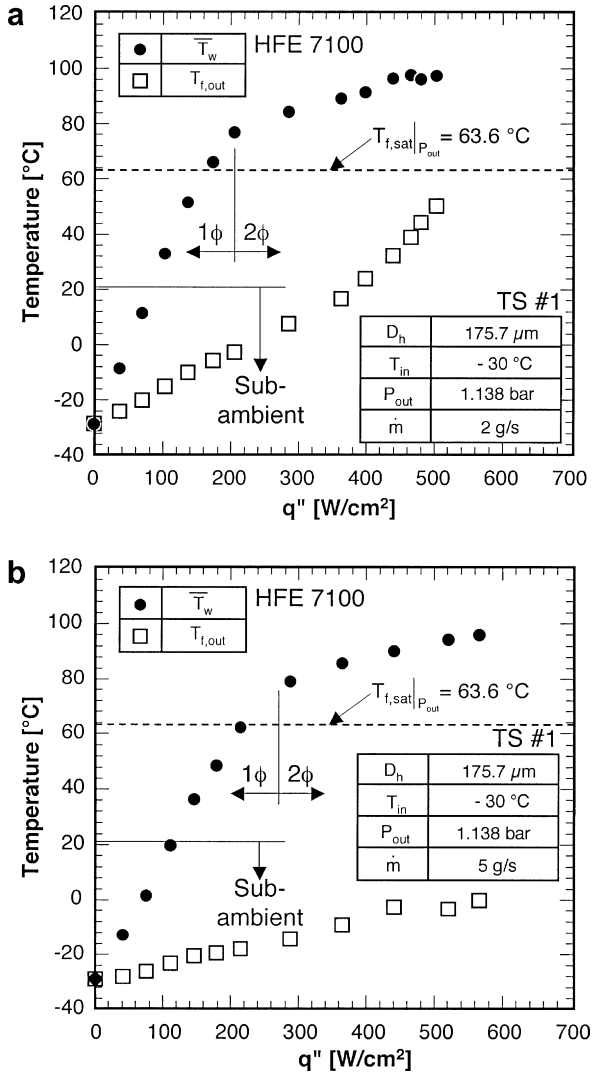

Fig. 5. Variations of measured fluid outlet temperature and mean micro-channel bottom wall temperature with heat flux for TS #1 at (a) $\dot{m} = 2$ g/s and (b) $\dot{m} = 5$ g/s.

3.2. Representative boiling curves

Fig. 6 shows subcooled boiling curves for TS#3 for inlet temperatures of −30 and 0 °C. Despite the similarity in boiling curve shape, appreciable differences in subcooled boiling behavior are observed between the two cases.

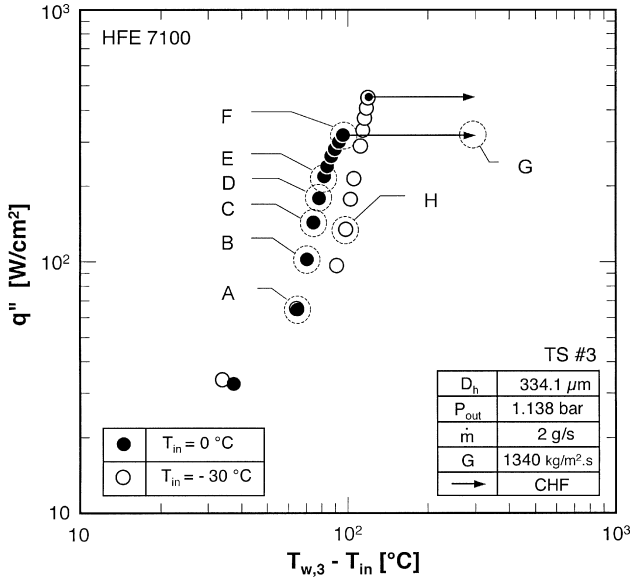

Fig. 6. Subcooled boiling curves for TS #3 for two inlet temperatures. Specific data points are indicated where video images of subsequent figures were captured.

Indicated in Fig. 6 are several data points ('A' to 'F') for $T_{in} = 0$ °C, spanning conditions between the onset of boiling and CHF. Point 'G' for the same inlet temperature corresponds to conditions during the transient that followed CHF. For comparison purposes, point 'H' corresponds to subcooled boiling conditions for $T_{in} = -30$ °C. Because of highly subcooled state at this lower temperature, boiling behavior showed far less variation with heat flux than at 0 °C. Representative video images that were captured at these points are presented and discussed in the following sections.

4. Flow visualization results

4.1. Nucleate boiling region

Fig. 7a shows initial bubble formation corresponding to point 'A' in Fig. 6. This is the point where the slope of the boiling curve increases sharply due to transition between the single-phase and the nucleate boiling regions. Because of limitations in focal range of the microscope lens used with the video camera, the channel length is shown divided into three regions, inlet, middle and outlet. There is slight overlap of the captured length of the middle region with both the inlet and outlet regions. Fig. 7a shows early nucleation does not occur uniformly in all micro-channels. Some channels contain an abundance of bubbles while others show no bubbles at all. However, even in the more bubble-populated micro-channels, bubbles appear to maintain fairly large separation distances, precluding any coalescence that might lead to axial growth in void fraction. It should be emphasized that the bubbles depicted in Fig. 7a do not necessarily correspond to their nucleation site or location of the nucleation site relative to the micro-channel's cross-section. A lateral force associated with the velocity profile across the liquid tends to keep bubbles in the vicinity of the micro-channel walls [10]. While the video images do not depict the location of bubbles relative to micro-channel depth, it is expected bubble growth favors the bottom wall where liquid is warmest.

Fig. 7b shows flow boiling images corresponding to point 'B' in Fig. 6. Here, with a higher heat flux, increased liquid superheat near the wall increases the number of active nucleating sites, resulting in more bubbles along the micro-channels. The increased superheat also allows bubbles to grow to a large diameter than at point 'A'. Notice that the ratio of bubble separation distance to bubble diameter decreases appreciably from point 'A', increasing the likelihood of bubble coalescence in the outlet region. It should also be noted that with the increased wall superheat, bubble nucleation is evident in all the micro-channels.

Fig. 7c shows images corresponding to point 'C' in Fig. 6. With this yet higher heat flux, increased wall superheat precipitates an increase in the number of active nucleating sites and therefore number of bubbles along the micro-channel. The ratio of separation distance to bubble diameter is also smaller, meaning bubbles can more easily coalesce into larger ones. The outlet region in particular shows signs of appreciable coalescence, an early indicator of transition to slug flow. Nonetheless, bubbly flow is dominant for all three heat flux conditions corresponding to points 'A', 'B' and 'C'.

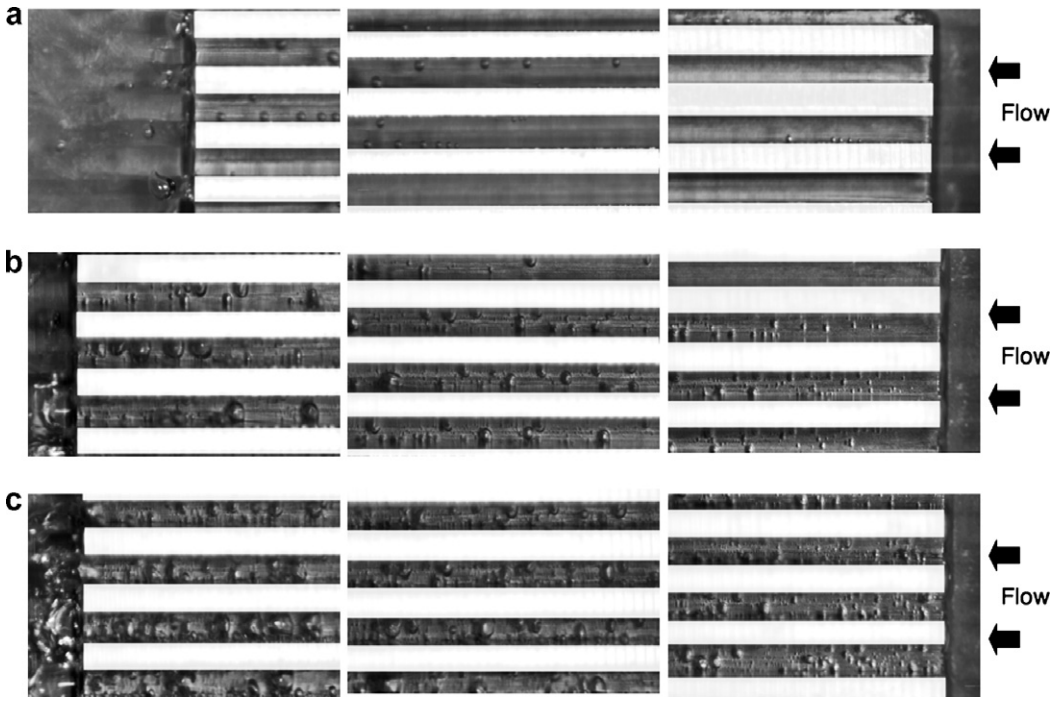

Fig. 7. Flow boiling images of inlet, middle and outlet regions for TS #3 ($D_h = 334.1$ μm) at $T_{in} = 0$ °C: (a) point 'A' ($q'' = 64.9$ W/cm^2), (b) point 'B' ($q'' = 102.3$ W/cm^2), and (c) point 'C' ($q'' = 142.8$ W/cm^2).

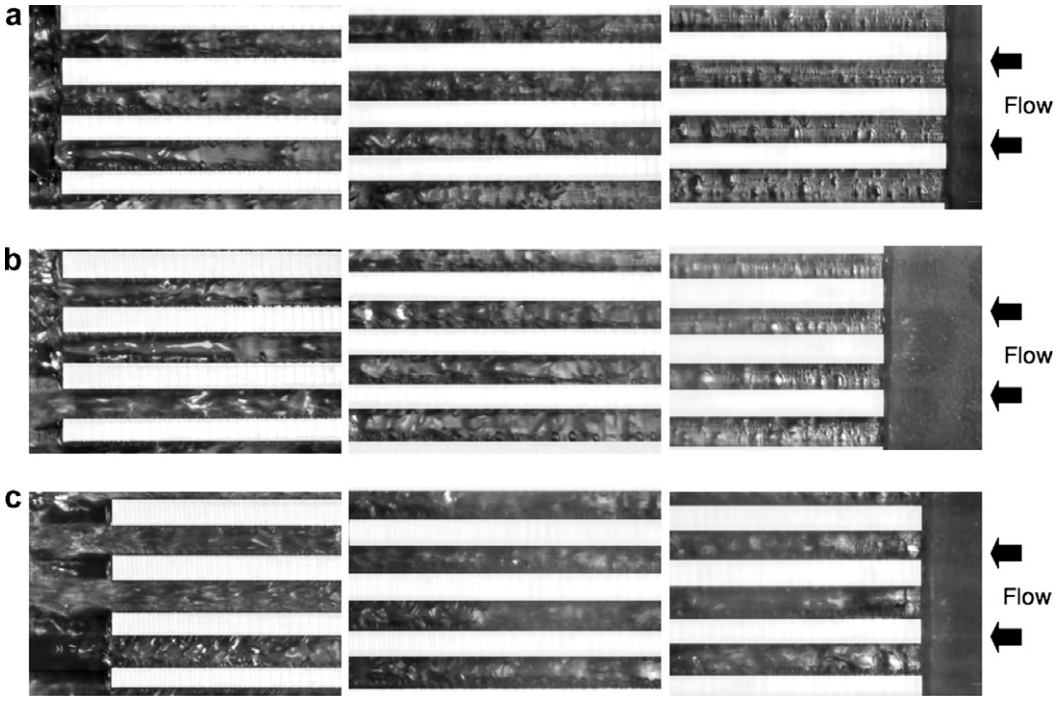

Fig. 8. Flow boiling images of inlet, middle and outlet regions for TS #3 ($D_h = 334.1$ μm) at $T_{in} = 0$ °C: (a) point 'D' ($q'' = 178.2$ W/cm^2), (b) point 'E' ($q'' = 218.3$ W/cm^2), and (c) point 'F' ($q'' = 318.3$ W/cm^2).

Fig. 8 depicts flow boiling images corresponding to further increases in heat flux. Here, further increases in wall superheat facilitate large increases in the number of bubbles nucleating upstream, as well as significant increase in void fraction, spurred mostly by coalescence of bubbles along the micro-channel. Fig. 8a shows oblong bubbles forming in the outlet region for point 'D'. Notice in the outlet regions both oblong slug flow bubbles and smaller discrete bubbles appear to form at the same axial location. This can be explained by differences in bubble behavior across the depth of the micro-channel. Because of the temperature gradient between the base and top of the micro-channel's cross-section, bubbles near the base are more likely to coalesce into large oblong bubbles, while smaller discrete bubbles near the top have less superheat to grow and coalesce. This shows the complexity of assigning a boiling regime for a given heat flux and axial location.

Fig. 8b shows the departure from bubbly to slug flow moves upstream to the middle region for point 'E'. There is also an appreciable increase in the length of slug flow bubbles in the outlet region, as well as a diminution in the number of small discrete bubbles in the same region.

4.2. Critical heat flux

For point 'F', Fig. 8c shows a further shift in the slug flow regime upstream toward the inlet. This point corresponds to the last steady-state condition in the nucleate boiling region before the onset of CHF. High stream-wise flow acceleration associated with the sharply increased void fraction causes coherent vapor jets to be ejected from the channel outlet. Unfortunately, lighting limitations on frame rate of the video camera precluded detailed resolution of interfacial activity in those jets.

CHF occurred when heat flux was increased slightly from point 'F'. Fig. 9a shows an image of the upstream region of the micro-channels that was captured while the heat sink temperature was escalating unsteadily. A thin layer of vapor is shown covering the micro-channel walls from the very inlet. As illustrated in Fig. 9b, abundant liquid is still visible in the core region fully separated from the micro-channel walls by the vapor layer. Capturing the video segment from which this image was obtained involved significant risk of physical burnout to the test section parts, especially the transparent polycarbonate cover plate. This is why it was difficult to obtain prolonged segments of this event.

4.3. Effects of subcooling

As discussed in the previous section, inlet temperature and, more importantly, inlet subcooling play a very important role in all aspects of bubble nucleation, growth and coalescence along the micro-channels. A reduced inlet temperature increases superheat in the vicinity of the micro-channel walls. As shown in Fig. 6, increased subcooling delays the onset of boiling to a higher heat flux. The effects of subcooling become readily apparent when comparing images in Fig. 10, which were captured at $T_{in} = -30$ °C, to those at $T_{in} = 0$ °C, Fig. 7c, for about the same heat flux. Strong condensation effects at −30 °C suppresses bubble growth and coalescence, prolonging the bubble growth

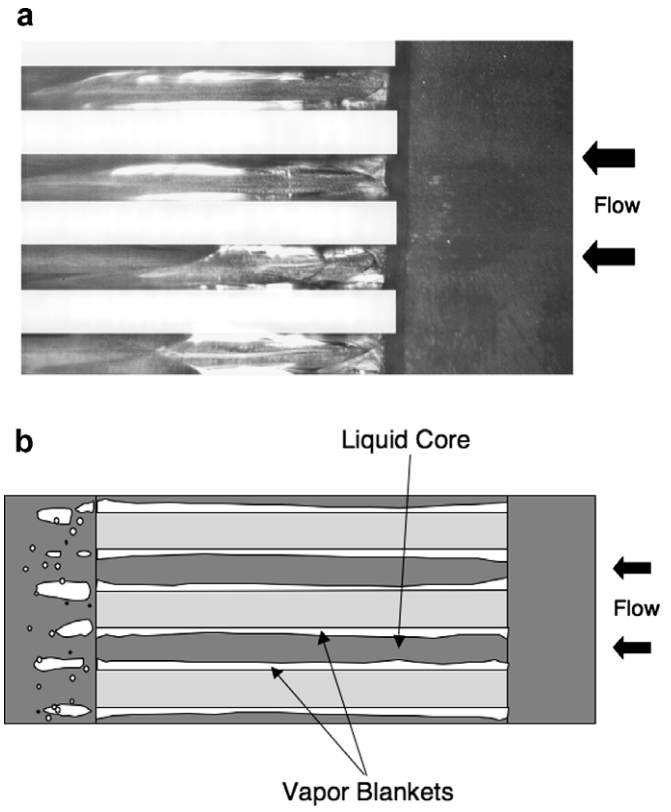

Fig. 9. (a) Flow image of inlet region for TS #3 ($D_h = 334.1$ μm) at $T_{in} = 0$ °C captured at point 'G' during transient following CHF. (b) Schematic representation of interfacial behavior at point 'G'.

regime and delaying transition to slug flow to much higher heat fluxes compared to 0 °C inlet temperature.

Another important effect of increased subcooling is the appreciable increase in CHF. Fig. 6 shows a CHF of 446.9 W/cm^2 for $T_{in} = -30$ °C compared to 318.3 W/cm^2 for $T_{in} = 0$ °C.

4.4. Effects of micro-channel geometry

The effects of micro-channel geometry are more complicated than those of subcooling. Fig. 11 depicts images obtained with TS #2 whose hydraulic diameter is $D_h = 200$ μm and width $W_{ch} = 123.4$ μm, as compared to $D_h = 334.1$ μm and $W_{ch} = 235.2$ μm for TS #3 depicted in Fig. 10. Fig. 11 corresponds to the same inlet temperature and heat flux, $T_{in} = -30$ °C and $q'' = 134$ W/cm^2, respectively, as Fig. 10, and about same mass velocity ($G = 1281$ kg/m^{2}s for Fig. 11 comparing to 1340 kg/m^{2}s for Fig. 10). Note that micro-channel width appears about equal in Figs. 10 and 11 because of the higher magnification lens used to capture images in Fig. 11. Only the middle region of the micro-channels was captured with this lens.

Fig. 11 shows far less bubble nucleation and coalescence than in Fig. 10. This may be explained by the 1.85 times greater wetted area for TS #2 compared to TS #3. The increased area both decreases the wall heat flux and wall superheat for TS #2, delaying the entire nucleation process. Another noticeable feature of boiling in TS #2 is increased

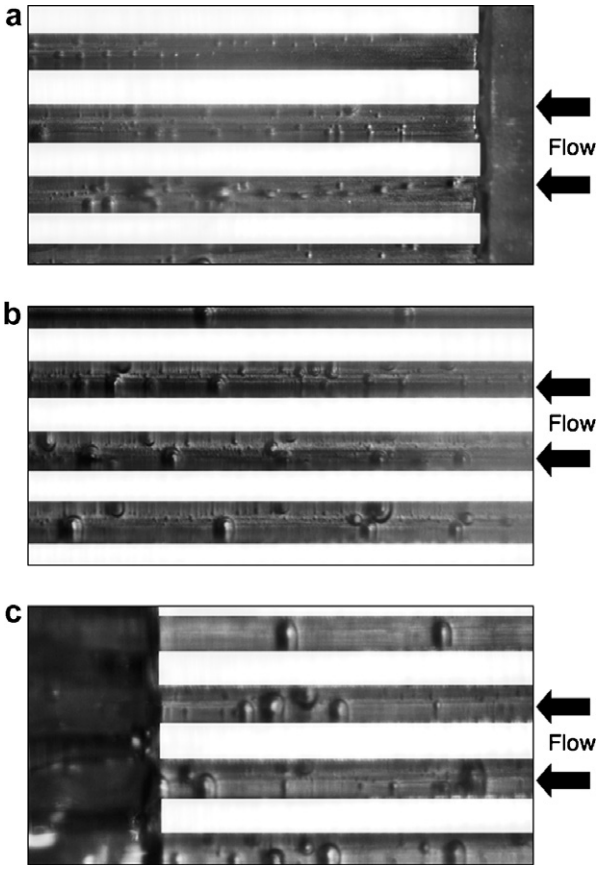

Fig. 10. Flow boiling images for TS #3 ($D_h = 334.1$ μm) at low temperature of $T_{in} = -30$ °C and $q'' = 134.0$ W/cm^2 corresponding to point 'H'. (a) Inlet region, (b) middle region, and (c) outlet region.

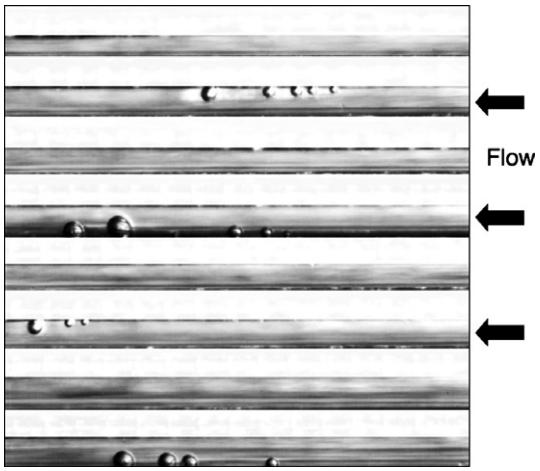

Fig. 11. Flow boiling image of middle region of micro-channel with smaller width and hydraulic diameter (TS #2, $D_h = 200$ μm) for $T_{in} = -30$ °C, $G = 1281$ kg/m^2 s, and $q'' = 134.0$ W/cm^2.

ratio of bubble size to micro-channel width despite the decreased wall superheat. Clearly visible in the middle micro-channel in Fig. 11 is a bubble whose size is two-thirds the micro-channel width. A yet smaller micro-channel width might promote the growth of bubbles that span the entire width of the micro-channel.

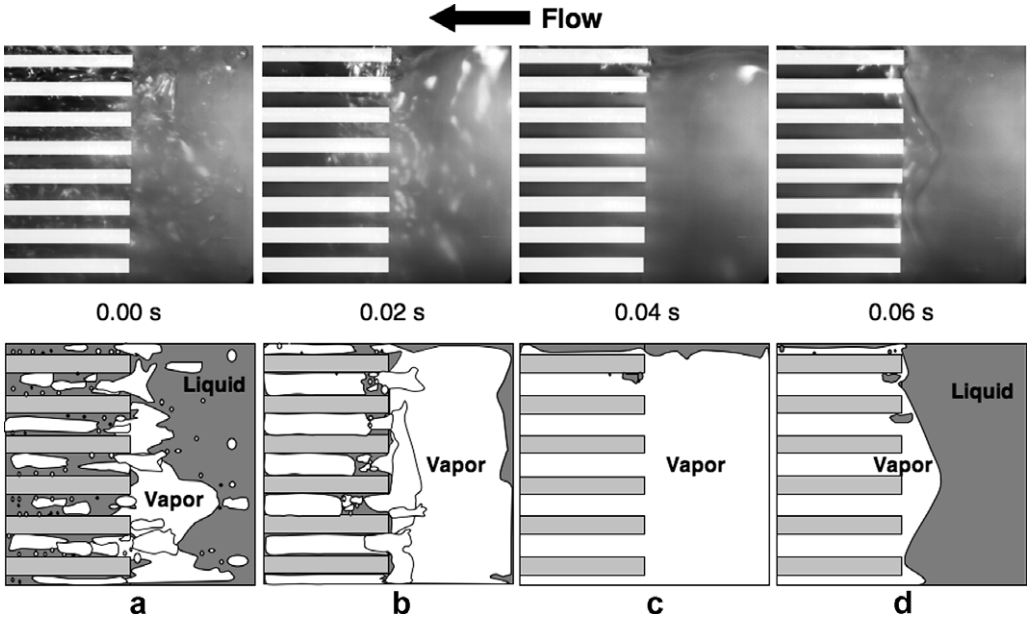

Fig. 12. Premature CHF and flow oscillations in TS #4 ($D_h = 415.9$ μm) for $T_{in} = 0$ °C, $G = 670$ kg/m^2 s, and $q'' > 250.0$ W/cm^2: (a) initial vapor pocket buildup in upstream plenum, (b) growth of vapor mass, (c) complete blockage of inlet plenum by vapor mass, and (d) purging of vapor mass along micro-channels.

Figs. 10 and 11 illustrate the complex combined influence of micro-channel geometry and subcooling. Both have drastic influence on the heat transfer performance of a micro-channel heat sink. The complexity of parametric influences highlights the need for mechanistic modeling of subcooled boiling in micro-channels.

4.5. Instabilities and premature CHF

The interfacial behavior discussed earlier in conjunction with Fig. 9 can be described as 'normal CHF' since it follows the mechanism of subcooled flow boiling CHF in large channels. However, a second drastically different type of CHF was encountered in the present study, which is best described as 'pre-mature CHF'. This type of CHF was associated with significant instability and flow oscillations.

Fig. 12 depicts a series of images separated by very short time intervals. Schematics of the same images are also shown to better explain interfacial behavior. A key difference between this case and those depicted in earlier figures is its much lower mass velocity, $G = 670$ kg/m^{2}s. With this lower mass velocity, a much larger volume of vapor is produced inside the micro-channels for the same inlet temperature and heat flux. This causes vapor coalescence into slug and even annular flow as far upstream as the inlet. With this low mass velocity, the momentum of incoming liquid in the upstream plenum is too weak to overcome the relatively large pressure drop exerted by the coalescing vapor. This causes vapor in the micro-channels to flow backwards towards the inlet plenum. Vapor from adjacent micro-channels then begins to merge into one large vapor mass inside the inlet plenum, momentarily blocking any incoming liquid from entering the micro-channels, and causing temporary dryout and temperature rise in the micro-channels. With this blockage, the upstream pressure gradually increases until it becomes high enough to push all the vapor mass downstream through the micro-channels, providing momentary wetting of the micro-channel walls and reducing wall temperature. This is followed by rapid vapor formation and coalescence inside the micro-channels and a repeat of the build-up/purge cycle. This cycle occurs with very high frequency and is associated with large fluctuations in both pressure and temperature. Conditions worsen with time as mean temperature increases with each new cycle. In fact, the peak temperature recorded by thermocouples in the copper heating block was about 200 °C when the images depicted in Fig. 12 were captured.

Fortunately, premature CHF can be prevented in two different ways. The first involves increasing the momentum of incoming liquid by increasing mass velocity. With sufficiently high liquid momentum, vapor backflow is prevented before it can even begin to accumulate a vapor mass in the upstream plenum. The second method is to lower the inlet temperature to take advantage of condensation and reduced bubble growth and coalescence. Both methods were proven in the present study to prevent the occurrence of premature CHF.

5. Conclusions

A new micro-channel cooling scheme is suggested where the primary coolant passing through the micro-channel heat sink is pre-cooled to low temperature using an indirect refrigeration cooling system. The cooling performance of this system was examined for different flow rates using four different micro-channel geometries. Extensive high-speed video imaging and photomicrography were used to capture

interfacial behavior with increasing heat flux up to and including CHF. Key findings from the study are as follows.

(1) Indirect refrigeration cooling is a highly effective means for removing heat from high-flux devices while maintaining low device temperatures. Unlike direct refrigeration cooling, where the micro-channel heat sink serves as evaporator in a vapor compression cycle, the present scheme decouples the quality requirements of the heat sink from those of the refrigeration loop. This decoupling alleviates compressor problems, facilitates high cooling capacity at low temperatures, and allows heat sink operation at near-ambient pressure.
(2) Cooling performance of the micro-channel heat sink can be greatly enhanced by lowering the temperature of coolant entering the heat sink. With temperatures of 0 °C or below, the heat sink could dissipate up to 100 W/cm^2 without phase change while maintaining surface temperatures below ambient. Heat fluxes as high as 700 W/cm^2 could be managed with flow boiling without the risk of burnout.
(3) Unlike most earlier two-phase heat sink studies, where annular film evaporation is the dominant mechanism for heat removal, the low coolant temperature used in the present study results in predominantly subcooled flow boiling, and outlet coolant temperature never reaches saturation. Some oblong bubbles typical of slug flow form mainly towards the outlet of the micro-channels. Decreasing the coolant temperature (*i.e.*, increasing subcooling) delays the onset of boiling, reduces bubble departure size and coalescence effects, and enhances CHF.
(4) CHF is associated with departure from nucleate boiling, caused by vapor blanket formation along the walls of the micro-channels even while abundant liquid is available in the core.
(5) Micro-channel hydraulic diameter and width play a complex role in cooling performance, and this role varies greatly with liquid subcooling. Small hydraulic diameter increases total wetted area, decreasing heat flux along the micro-channel walls. This tends to decrease void fraction along the micro-channels. On the other hand, a limit might be reached where decreasing micro-channel width causes bubbles to span the entire width and promote early transition to slug flow. These complex effects highlight the need for a comprehensive mechanistic model for subcooled flow boiling in micro-channel heat sinks.
(6) A premature form of CHF is associated with vapor flow reversal toward the inlet plenum. This is followed by development of a large vapor mass in the upstream plenum, which prevents liquid from flowing into the micro-channels. Momentary dryout ensues inside the micro-channels and wall temperatures begin to rise. The vapor buildup causes an increase in the upstream pressure, which ultimately becomes strong enough to purge the vapor mass through the micro-channels and into the outlet plenum. This process is then repeated in a cyclical manner as wall temperatures continue to rise gradually with each new cycle. This form of CHF occurs only at low mass velocities and can be eliminated by decreasing coolant temperature and/or increasing flow rate.

Acknowledgement

The authors are grateful for the support of the Office of Naval Research (ONR) for this study.

References

[1] I. Mudawar, Assessment of high-heat-flux thermal management schemes, IEEE Trans.-CPMT Comp. Pack. Technol. 24 (2001) 122–141.
[2] J.W. Peeples, W. Little, R. Shcmidt, M. Nisenoff, Low temperature electronics workshop, in: Proceedings of 16th Semiconductor Thermal Measurement and Management Symposium, IEEE, San Jose, CA, 2000, pp. 108–109.
[3] R.R. Schmidt, B.D. Notohardjono, High-end server low-temperature cooling, IBM J. Res. Dev. 46 (2002) 739–751.
[4] R.K. Kirschman, Cold electronics: an overview, Cryogenics 25 (1985) 115–122.
[5] J. Lee, I. Mudawar, Two-phase flow in high-heat-flux micro-channel heat sink for refrigeration cooling applications: Part I – Pressure drop characteristics, Int. J. Heat Mass Transfer 48 (2005) 928–940.
[6] J. Lee, I. Mudawar, Two-phase flow in high-heat-flux micro-channel heat sink for refrigeration cooling applications: Part II – Heat transfer characteristics, Int. J. Heat Mass Transfer 48 (2005) 941–955.
[7] J. Lee, I. Mudawar, Implementation of microchannel evaporator for high-heat-flux refrigeration cooling applications, ASME J. Electron. Pack. 128 (2006) 30–37.
[8] W. Qu, I. Mudawar, Flow boiling heat transfer in two-phase micro-channel heat sinks – I. Experimental investigation and assessment of correlation methods, Int. J. Heat Mass Transfer 46 (2003) 2755–2771.
[9] W. Qu, I. Mudawar, Measurement and prediction of pressure drop in two-phase micro-channel heat sinks, Int. J. Heat Mass Transfer 46 (2003) 2737–2753.
[10] C.H. Lee, I. Mudawar, A mechanistic critical heat flux model for subcooled flow boiling based on local bulk flow conditions, Int. J. Multiphase Flow 14 (1989) 711–728.